Journal of ELECTRONIC MATERIALS, Vol. 49, No. 1, 2020
https://doi.org/10.1007/s11664-019-07751-0

Investigation on Microstructural, Electrical and Optical Properties of Nd-Doped $BaCo_{0.01}Ti_{0.99}O_3$ Perovskite

K. MADHAN[1] and R. MURUGARAJ[1,2]

1.—Department of Physics, MIT Campus, Anna University, Chennai 600044, India. 2.—e-mail: r.murugaraj@gmail.com

The effects of microstructural, electrical and optical properties of $(Ba_{1-x}Nd_x)(Co_{0.01}Ti_{0.99})O_3$ (BNCT) ($x = 0.00\%$, 0.25%, 0.50% and 0.75%) ceramics have been prepared the by sol–gel combustion technique. The structural phase evolution confirms tetragonal to pseudo-cubic phase with 0.50% and 0.75% doping of Nd^{3+} ions. The Rietveld refinement analysis of BNCT ceramics in terms of bond length Ba-O, Ti-O and Ba-Ti have been discussed, and it also confirmed the lattice parameters systematically. The co-doping of Nd^{3+} ions for Ba^{2+} ion at A-site leads to an increase of the energy bandgap (E_g) of the samples lying between 2.93 eV to 3.19 eV, which is ascertained by the blue shift as observed from the UV–visible spectroscopy. The intensity of photoluminescence (PL) emission was found to decrease with an increase in Nd^{3+} concentrations and the deconvolution of the luminescence peaks were discussed in terms of the role of defects, oxygen vacancies, grain size, and induced lattice strain. The complex permittivity ($\varepsilon' + j\varepsilon''$), impedance plot and AC conductivity (σ') were examined at room temperature within the frequency range from 1 Hz to 1 MHz.

Key words: Sol–gel processes, defects, optical properties, electrical properties, spectroscopy

INTRODUCTION

Ferroelectric ceramics with perovskites lattice structure are vital materials due to their intricate physical properties and widespread technological applications. In particular, barium titanate is regarded as the basis and prototype structure of valuable ferroelectrics for device applications.[1] In the past few decades, $BaTiO_3$ has been widely used for device applications such as optoelectronic devices, pulse generating devices, transducers, capacitors, resistors, thermal sensors, electrostriction devices, infrared detectors, phase transitions, electro-optic devices, etc.[2,3] From the review of the literature, it has been observed that these physical and chemical technological properties of $BaTiO_3$ are sensitive to the variations of contiguous temperature, impurities, crystal structure, crystallite size and defect densities.[4–7] Also, $BaTiO_3$ can exist in different structures such as rhombohedral (< − 90°C), orthorhombic (− 90°C to 5°C), tetragonal (0–130°C) and cubic structure from the Curie temperature (130°C) and above 1460°C its transformation into hexagonal phase.[1,2,7] In addition, at Curie temperature, $BaTiO_3$ undergoes ferroelectric–to–paraelectric transition.[8] In accumulation, the dielectric and semiconducting properties of $BaTiO_3$ ceramics can be modified by the addition of suitable oxides in an effective way to enhance their role in potential applications.[9] In particular, the rare-earth oxide is one of the most important additives of $BaTiO_3$ for potential applications. The ionic radius of the substituting rare-earth ion is an important parameter, which mainly determines the incorporation site and sequentially through the physical properties. Generally, the rare-earth elements with larger ionic radius, such as Nd^{3+} (1.27 Å) replace Ba^{2+} (1.61 Å) and Co^{3+} (0.65 Å) as their ionic sizes

---

(Received July 15, 2019; accepted October 18, 2019;

are compatible with that of Ti^{4+} (0.605 Å) and maintain the charge compensation. Hence, doped BTO results in the structural phase transition with an enhancement of optical and electrical properties up to a certain doping percentage.[10–12]

In general, transition metal ions have several oxidation states, further doping of transition metal like Fe, Co ions at Ti-site may influence conduction and exchange interaction between different elements or different valence states of the same elements, which helps to augment both the electrical and magnetic properties.[9] In other words, Nd and Co ions are used as a donor type dopant in $BaTiO_3$ and the formation of donor–acceptor complexes will enhance the electrical and optical properties of $Ba_{1-x}Nd_x(Ti_{0.99}Co_{0.01})O_3$ ceramics. However, the donor type dopant at high concentration is explained by either electronic compensation with lower concentrations of Nd^{3+} ion or oxygen-related vacancies. For higher dopant concentrations, the grain boundaries reduce grain growth. Increasing grain boundary with an increase in donor concentration leads to changes electronically to vacancy compensation in the materials.[13]

In light of the above properties, in the present work, we prepared $(Ba_{1-x}Nd_x)(Ti_{0.99}Co_{0.01})O_3$ ceramics with different Nd-doping concentrations using the sol–gel combustion method. In the present case, the Ba^{2+} ions are substituted by Nd^{3+} ion at A-site (off-valent), which can lead to an A-site disordered cation with defect structure. These result in a blue shift in optical absorption, which depends on the carrier concentration as investigated. The determinations of this exploration are studied through the effect of Nd^{3+} ions on the structural, optical and electrical properties of the modified BNCT ceramics that were investigated and the observed results are reported.

EXPERIMENTAL DETAILS

$(Ba_{1-x}Nd_x)(Co_{0.01}Ti_{0.99})O_3$ (x = 0.00%, 0.25%, 0.50% and 0.75%) ceramics were prepared using the sol–gel combustion technique with proper stoichiometric proportions of $(C_{12}H_{28}O_4Ti)$, $(Co(NO_3)_2)$, Nd_2O_3 $(Ba(NO_3)_2)$ that were taken as a starting reagent. Glacial acetic acid and ethanol were used as solvents for the above mixtures. Titanium (IV) isopropoxide was added very slowly to the clear mixture solution with continuous stirring to obtain a yellowish solution. This solution was added together into deionized water to complete the hydrolysis process. The mixed final solution was continuously stirred in a hotplate at 80°C for 4 h. Subsequently, the wet gel was formed through the combustion process, and the resultant powder was calcined at 900°C for 3 h.

The powder x-ray diffraction (XRD) was analyzed using a Bruker-D2 phaser diffractometer with radiation of Cu-Kα having wavelength λ = 1.5418 Å and step size of 0.02° for the 2θ from 10° to 80° to confirm the phase formation. The XRD pattern of Rietveld refinement profile fitting was analyzed by the *GSAS & EXPUGI* software package.[14] The Raman spectra are analyzed using a Raman spectrometer (LabRamHR) with excitation laser wavelength 514 nm. The surface morphology with a grain size of the synthesized ceramics was analyzed using an High-resolution Scanning Electron Microscope (HRSEM), which was recorded at ambient temperature using a Quanta 200 FEG scanning electron microscope. Grain size distributions were calculated using *Image j* analyzing software and plotting as log-normal distribution in the form of a histogram. The diffuse reflectance spectra (DRS) were recorded at ambient temperature by an UV–visible Spectrometer (Shimadzu UV 2450 PC Spectrophotometer) and the band gap was achieved using a *tauc plot*. The photoluminescence analyses were obtained using a fluorescence spectrometer (Varian Cary Eclipse) with an excitation source of 435 nm. In this work, PL spectra were fitted with a Gaussian function independently and individual peaks were obtained through the deconvolution process by *Fityk software*.[15] For dielectric measurements, the samples were pelletized with the dimensions of 8 mm (dia) and 1 mm (thickness), sintered at 900°C, and for the electrode contact silver paste was coated on both sides of the pellet. The frequency-dependent dielectric measurements were carried out on the sintered pellets by employing PSM1735NumetriQ. The observed results are discussed in detail below.

RESULTS AND DISCUSSION

XRD Analysis

Figure 1 illustrates the XRD patterns of BNCT samples recorded at ambient temperature. A structural phase evolution is observed as tetragonal to pseudo-cubic phase on increasing Nd^{3+} ion concentrations at 0.50% and 0.75%. The perovskite structure of BNCT ceramics was analyzed by Rietveld refinement and the observed results in terms of bond length and lattice parameters have been analyzed. In order to reveal it, the lattice parameters of ceramic samples are deliberated in Table I. It is noteworthy that the observed patterns are very good matches with the calculated patterns as a result of comparatively lesser residuals for the weighted patterns R_p and R_{wp} values. In addition, the lattice parameters, residual factors, the goodness of fit (R_{wp}, R_P, and χ^2), bond lengths and unit cell volume were obtained from the refinement and are listed in Table I. In ABO_3 structure, the Co^{3+} (0.65 Å) ions are doped in the Ti^{4+}-site (0.605 Å) because of the similar ionic radii. Further, Nd^{3+} (0.98 Å) are doped in the A-site, as it enters into the lattice site of Ba^{2+} (1.36 Å) ions due to the comparable coordination number and difference in the ionic radii of Nd^{3+} and Ba^{2+} ions.[16–18] The ionic radii of Ba^{2+} that are greater than the Nd^{3+} leads to an increase in the bond length of Ba-O in the BNCT ceramics. Further, the doping of Ti^{4+} ions is compared to the Co^{3+} ions, which results in a reduced bond length between A-site (Nd^{3+} ion) and O^{-2} as related to the Ba-O bond. It is realistic that Nd^{3+} ions completely entered the BNCT lattice as observed from our results. However, when the content of Nd^{3+} increased it might be replaced by a Ti^{4+} ion, which lead to an increase in unit cell volume. From Table I, it is observed that the Ti-O bond lengths at the octahedron site are approximately equal to two. The lattice parameters (a, b and c) obtained from the refinement are found to decrease with doping ion concentration from $x = 0.25\%$ to 0.75% which may be due to induced strain in the BTO lattice.

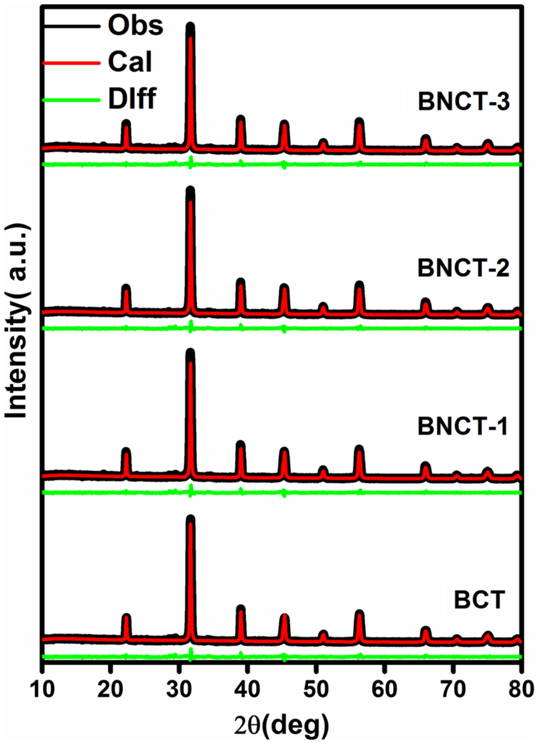

Fig. 1. Powder XRD pattern with Rietveld refinement of $(Ba_{1-x}Nd_x)(Co_{0.01}Ti_{0.99})O_3$ (BCT), (BNCT-1 $x = 0.25\%$), BNCT-2 $x = 0.50\%$) (BNCT-3 $x = 0.75\%$).

Microstructure (HRSEM) Analysis

The HRSEM images of BNCT ferroelectric ceramic materials are recorded at ambient temperature for various doping concentrations of Nd^{3+} ions as illustrated in Fig. 2a, b, c, and d, respectively. The microstructure of BNCT exhibits a large number of grains with aggregated polygonal shape and some grains show a possible draw line on polygonal shape and pyramid shape. As increasing Nd^{3+} ions, the grain sizes are found to be decreased and grains are randomly oriented in the doped BCT system. These observed surface morphological images confirm the average grain size decreases with the addition of Nd^{3+} ion to BCT ceramics. The inhibition of smaller grain size may be due to the smaller ionic radii of Nd^{3+} ion.[11]

Optical Analysis

UV–Visible Spectroscopy and Estimation of the Energy Band Gap

The UV–visible absorption spectra for BCT and BNCT perovskite samples were probed by means of diffuse reflectance spectroscopy (DRS) technique and the observed results are shown in Fig. 3a. The diffuse reflectance spectra of prepared BNCT ceramic materials is against a reference standard material $BaSO_4$ compound in the wide range of 200–800 nm wavelengths. It was apparent that on increasing Nd^{3+} ion doping concentration in BNCT ceramics, the maximum absorption was found to shift towards higher wavelength, which signifies the

Table I. Powder XRD Rietveld refinement factors of $(Ba_{1-x}Nd_x)(Co_{0.01}Ti_{0.99})O_3$(BCT), (BNCT-1 $x = 0.25\%$), BNCT-2 $x = 0.50\%$), (BNCT-3 $x = 0.75\%$)

Sample	BCT	BNCT-1	BNCT-2	BNCT-3
Crystallite size (nm)	70	53	46	43
Lattice strain (10^{-3})	2.2	2.3	3.6	5.7
X-ray density (gm/cm^3)	6.199	5.702	5.929	6.489
Lattice parameters				
a (Å)	4.0031	4.0038	4.0017	4.0113
c (Å)	4.0198	4.0176	4.0014	3.9999
c/a	1.0041	1.0034	0.999	0.997
Cell volume (Å^3)	64.420	64.405	64.283	64.365
R-factor (%)				
R_p	6.01	5.35	5.28	5.81
R_{wp}	7.80	7.19	7.09	7.91
χ^2	2.65	2.40	2.30	2.92
Bond length (Å)				
Ti-O	1.990(9)	2.015(5)	2.003(6)	2.002(13)
Ba-O	2.802(4)	2.831(5)	2.833(6)	2.832(13)
Ba-Ti	3.402(12)	3.554(12)	3.469(8)	3.469(17)

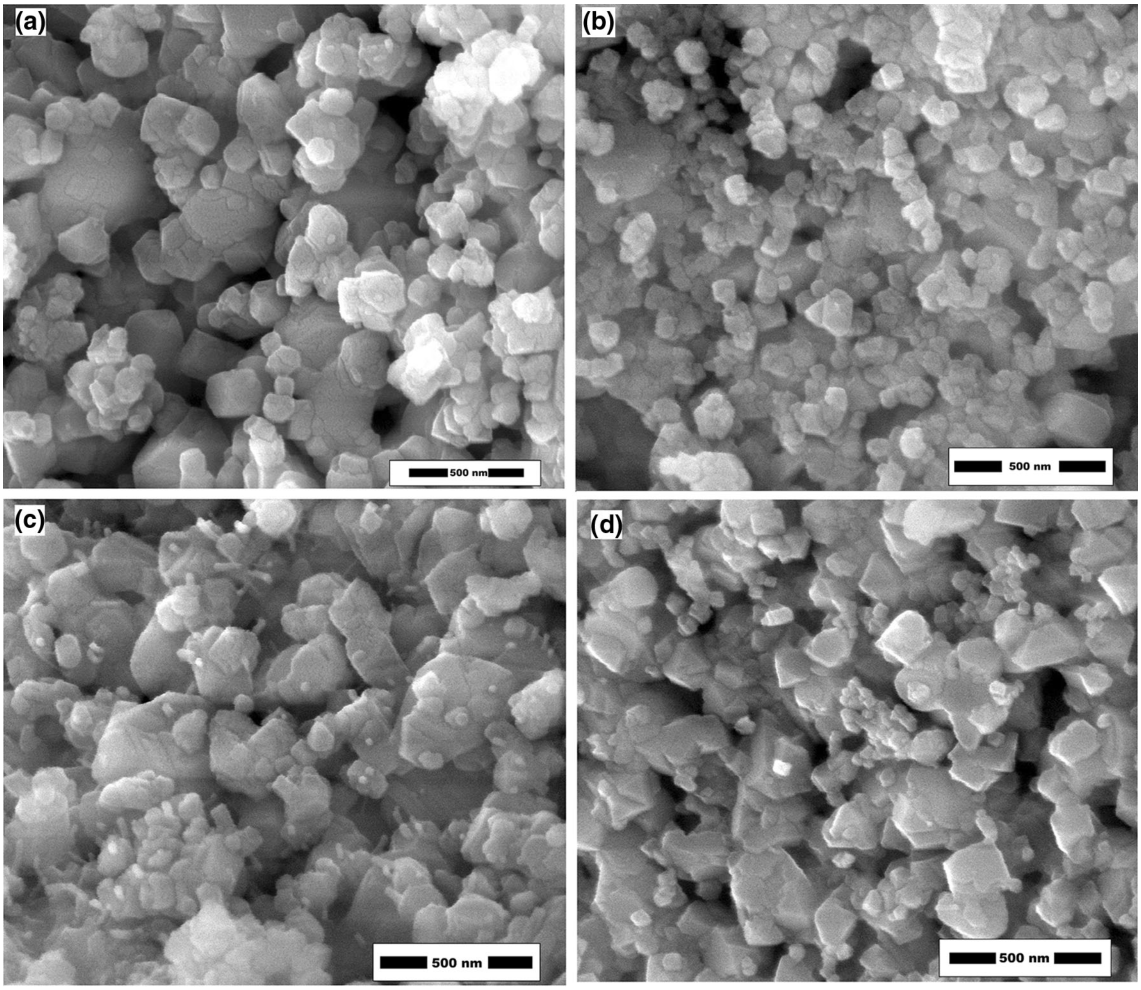

Fig. 2. HR SEM images of $(Ba_{1-x}Nd_x)(Co_{0.01}Ti_{0.99})O_3$ (a-BCT), (b-BNCT-1), (c-BNCT-2) (d-BNCT-3).

strong optical absorption behavior of the samples. In the UV–Vis absorption spectra of BNCT ceramics, the peaks corresponding to typical Co^{3+} transitions are observed and ligand–metal charge transfer movements $O^{2-} \rightarrow Co^{3+}$ and $O^{2-} \rightarrow Co^{2+}$ at 554 nm. The optical absorption behavior of BNCT samples exposes the influence of crystallite size, grain size and lattice strain in the samples.[19]

The optical energy band gap was estimated from the diffuse reflectance spectra and is shown in Fig. 3b. The equivalent absorption spectra using the ***Tauc*** function of absorption coefficient α and optical band gap E_g is expressed as

$$hv = (hv - E_g)^n, \quad (1)$$

where 'h' is Planck's constant, 'v' is the frequency of incident radiation and n = ½ for the direct and n = 2 for the indirect bandgap semiconductor materials. The optical energy bandgap (E_g) values were correlated with factors such as temperature, surface morphology and preparation methods of the ceramic materials.[20] The estimated band gap values varied from 2.93 eV to 3.19 eV for BNCT at various concentrations. Similarly, the estimation of charge carrier concentrations (n_e) from the bandgap, which originates from charge transfer and raises its value from 0.947×10^{20} cm^{-3} to 1.208×10^{20} cm^{-3} upon doping of Nd^{3+} ion concentrations, has the observed results reported in Table II. It is identified that the effect of doping along with particle size greatly influences electronic parameters like energy bandgap and carrier concentrations. However, the decrease in the tetragonality phase with increasing Nd^{3+} ion doping concentrations, the influence of the interaction on the bandgap is gradually increased. From Table II, it is observed that there is the increase of bandgap and carrier concentration values with increasing the doping content of Nd^{3+} in BCT compounds. In addition, the bandgap of perovskites can also be increased through tetragonal to pseudo-cubic structural phase transition.[21] In the present case, the Nd^{3+} ion concentration was increased and the observed band gap (E_g) also gradually increases for the variation of dominated phase transition. These types of variation in energy band gap values occur due to the order–disorder

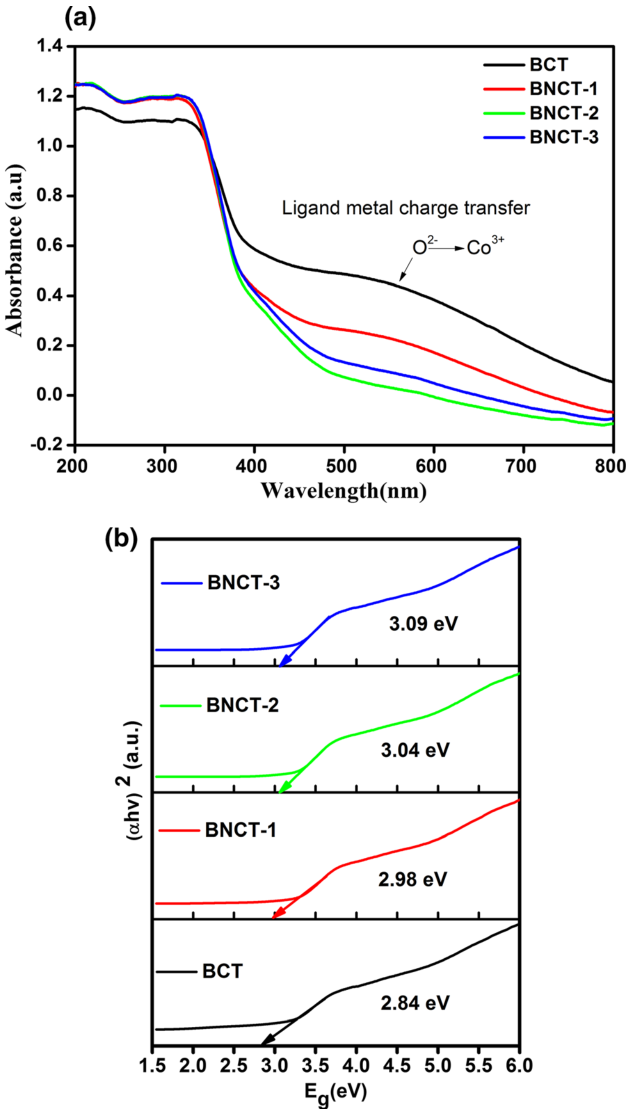

Fig. 3. (a) UV DRS spectra of $(Ba_{1-x}Nd_x)(Co_{0.01}Ti_{0.99})O_3$ (BCT), (BNCT-1 $x = 0.25\%$), BNCT-2 $x = 0.50\%$) (BNCT-3 $x = 0.75\%$). (b) UV optical band gap of $(Ba_{1-x}Nd_x)(Co_{0.01}Ti_{0.99})O_3$ (BCT), (BNCT-1 $x = 0.25\%$), BNCT-2 $x = 0.50\%$) (BNCT-3 $x = 0.75\%$).

Table II. The near energy band edge (NBE) emission, Band gap (E_g) and Carrier concentration (n_e), of $(Ba_{1-x}Nd_x)(Co_{0.01}Ti_{0.99})O_3$ (BCT), (BNCT-1 $x = 0.25\%$), BNCT-2 $x = 0.50\%$) (BNCT-3 $x = 0.75\%$)

NBE E_{PL} (eV)	Band gap E_g (eV)	Carrier concentration $n_e \times 10^{20}$ (cm^{-3})
2.313	2.84	0.947
2.315	2.98	1.095
2.319	3.04	1.162
3.320	3.08	1.208

factor, which is ascribed due to the presence of impurities or distortions of TiO_6 octahedra and oxygen-related vacancies.[22]

Luminescent Properties

PL is one of the most extensive studies used to scrutinizing the intermediate energy levels within the energy band gap and determining the degree of ordered-disordered structure. The ambient temperature PL spectra of BNCT samples are shown in Fig. 4. In general, for the ABO_3 structure, the PL emission occurs due to the polarization of some localized states in the bandgap, self-trapped excitons, oxygen vacancies which are the mainly dominant defect centers and formation of oxygen vacancies related to freeing of charge carriers.[23] The BCT and Nd^{3+} doped BCT samples clearly showed that the three strongest emission peaks, viz., green (532 nm), orange (595 nm) and red (717 nm) are as observed in this spectrum. It was analyzed using ***Fityk software*** by the Gaussian deconvolution process and depicted in Fig. 4. The wavelength region of the fitted curves through Gaussian fit independently, the each and individual peaks are attained through the de-convolution process and exposed in Table III.[24–26] The visible PL emission specifies the more ordered and disordered structure of ABO_3 materials, and it is observed in green, orange and red emissions.[27,28] The visible green emission band as observed at 532 nm was due to the presence of host lattice oxygen vacancies or by lattice defects due to the self-activated phosphor type luminescence, which can be realized in the perovskite systems.[29] The near energy band edge (NBE) emission of the BNCT system measures the bandgap energy (E_{PL}). Further, the increase of Nd^{3+} ion dopant concentrations leads to shifting of the strong emission peak from 520 nm to 545 nm with an increase in the bandgap value from 2.312 eV to 2.320 eV as observed from Table II. This type of similar behavior was observed in UV-absorption spectral analysis. Therefore, the obtained PL spectra independently prove the existence of oxygen-related vacancies which are due to the defects in shallow donor level near the conduction band and defect states. The oxygen vacancies were observed as highly localized sensitive centers to trap the electrons from the valence band and then the interaction of this electron trapped with holes form self-trapped excitations. The intensity of the emission increased progressively, representing decreasing of oxygen vacancies related defects with the increasing doping of Nd^{3+} ions.[30]

Dielectric Analysis

Figure 5a and b show the effect of frequency with the real part of dielectric constant (ε') andthe imaginary part of dielectric loss (ε'') obtained from 1 Hz to 1 MHz for $(Ba_{1-x}Nd_x)(Co_{0.01}Ti_{0.99})O_3$ (BNCT) ($x = 0.00\%$, 0.25%, 0.50% and 0.75%) ceramics at ambient temperature. From Fig. 5a, we observed that the ε' reduced with an increase of frequency, which is constant with the collective response of orientational relaxation of induced

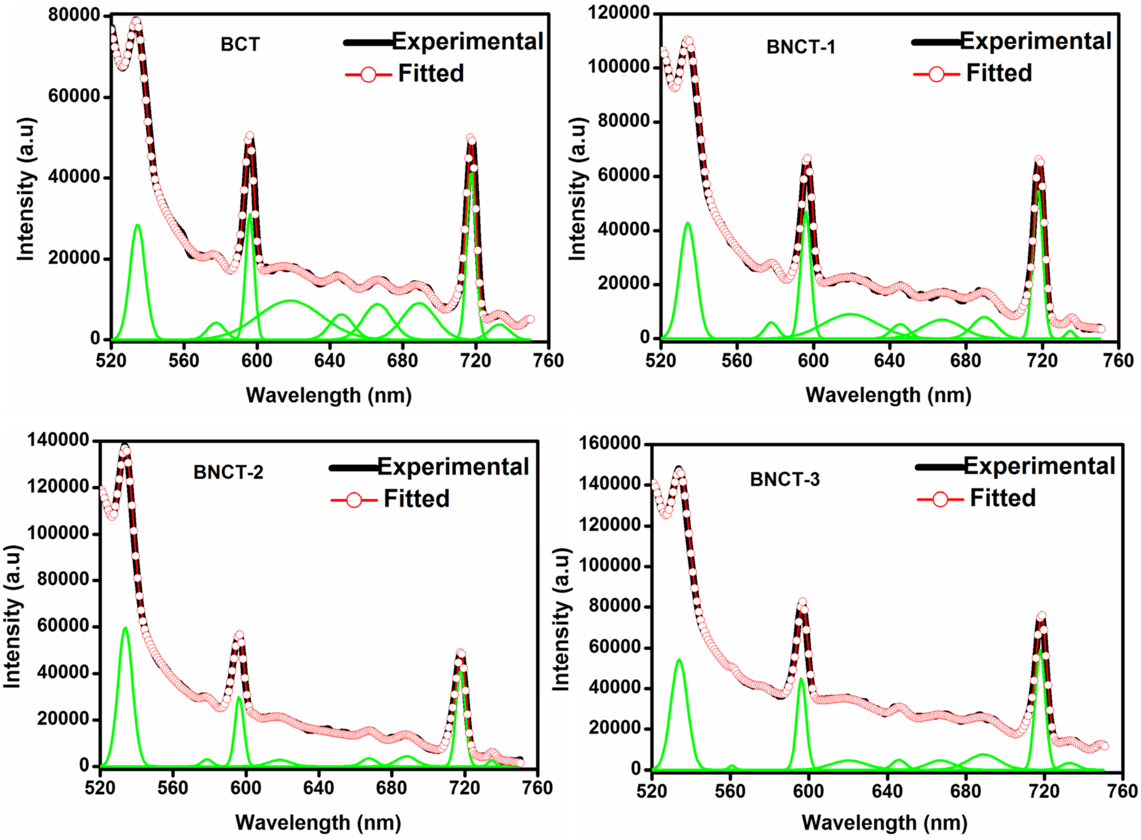

Fig. 4. PL spectra of $(Ba_{1-x}Nd_x)(Co_{0.01}Ti_{0.99})O_3$ (BCT), (BNCT-1 $x = 0.25\%$), BNCT-2 $x = 0.50\%$) (BNCT-3 $x = 0.75\%$).

Table III. PL modes and full width at half maxima of $(Ba_{1-x}Nd_x)(Co_{0.01}Ti_{0.99})O_3$ (BCT), (BNCT-1 $x = 0.25\%$), BNCT-2 $x = 0.50\%$) (BNCT-3 $x = 0.75\%$)

PL peaks (nm)				FWHM (nm)			
BCT	**BNCT-1**	**BNCT-2**	**BNCT-3**	**BCT**	**BNCT-1**	**BNCT-2**	**BNCT-3**
534.198	533.842	532.813	532.692	4.897	5.087	4.669	4.946
596.131	596.696	596.129	597.301	2.811	3.089	2.851	2.798
718.198	718.186	717.552	718.672	3.003	2.988	2.959	3.028

dipoles and charge carrier conduction. At the low-frequency region, its space charge, atomic, dipolar and electronic polarization follows the applied electric field. However, in the high-frequency region, only ionic and electronic polarization can follow the applied electric field and other polarizations are not able to follow and behave as static naturally. The dispersive behavior dielectric constants with frequency are due to the Maxwell–Wagner type polarization, which agrees with Koop's phenomenological theory.[5,31] At 1000 Hz frequency, the value of ε' has been found to 3268, 3314, 4909 and 12128 for different doping concentrations at ambient temperature. The enhancement of dielectric constants on increasing Nd^{3+} ion doping leads to a change in the particle size and interactions between free carrier concentrations.[32]

The dielectric loss (ε'') as exposed in Fig. 5b, exhibits the energy loss in the dielectric materials which is also reduced with higher frequencies. In lower frequency regions, the value of ε'' appears to be in decreasing trends, due to the dipole contribution towards polarization.[5,33] This decrease in loss factor with an increase in Nd^{3+} doping is attributed to improving the dielectric properties of BCT with Nd^{3+} ion doping. The increase of free carrier concentrations and the reduction of oxygen vacancies are also responsible for the increasing ε' and decreasing of ε'' upon the doping of Nd^{3+} ion in BCT compounds.[34]

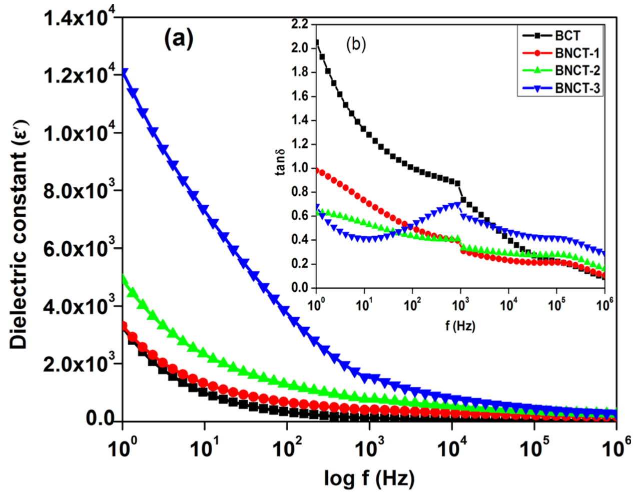

Fig. 5. (a) dielectric constant (b) loss of $(Ba_{1-x}Nd_x)(Co_{0.01}Ti_{0.99})O_3$ (BCT), (BNCT-1 $x = 0.25\%$), BNCT-2 $x = 0.50\%$) (BNCT-3 $x = 0.75\%$).

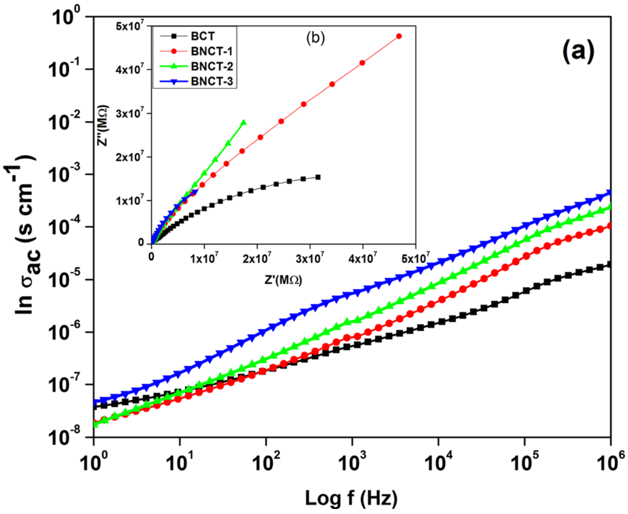

Fig. 6. (a) AC conductivity (b) impedance plot of $(Ba_{1-x}Nd_x)(Co_{0.01}Ti_{0.99})O_3$ (BCT), (BNCT-1 $x = 0.25\%$), BNCT-2 $x = 0.50\%$) (BNCT-3 $x = 0.75\%$).

AC Conductivity and Impedance Analysis

Figure 6a depicts the frequency dependence of the real part of the ac conductivity (σ') at ambient temperature for the present samples. From the conductivity dispersive curve, it is clearly noted that the conductivity $\sigma'(\omega)$ rapidly increases with the change in frequency. The power-law behavior is evident in the ac conductivity throughout the entire frequency range, because of the absence of a frequency-independent plateau region at the lower frequency regions.[35]

However, the plateau region slowly develops as an increasing trend of the Nd^{3+} ion doping, which is representing the activated nature of dc conduction in these compounds. The $\sigma'(\omega)$ values are found to be increased with an increase in Nd^{3+} ion content in BCT samples.[36] This increase in conductivity leads to an enhancement of the transition of charge carriers. In order to get more insight into the electrical conduction mechanisms, we have executed the impedance analysis through the complex plane plot of Z' versus Z'' (Nyquist plots) at ambient temperature which is shown in Fig. 6b. For Nd^{3+} ion-doped BCT samples (x = 0.00%, 0.25%, 0.50%, 0.75%), a clear semicircular arc could not be observed due to the high resistivity nature of the sample. For BCT samples, the reductions in the size of an arc reveal that the dielectric relaxations vary from the ideal Debye behavior. This deviation can be related to additional electrical conductivity due to the larger grain boundary volume in comparison to the smaller particle size.[37]

CONCLUSIONS

The effects of Nd^{3+} ion doping on BCT structural phase composition, microstructures and electro-optical properties have been investigated. The XRD analysis confirmed the phase transition in tetragonal to pseudo-cubic structure performed with increasing Nd^{3+} ion doping levels. In addition, the grain size of the BNCT samples was found to be decreasing with the increasing of Nd^{3+} ion content. The Nd^{3+} ions enter into Ba^{2+} ions at A-sites on doping, in addition to the above the Nd^{3+} ion to some extent can significantly decrease the grain growth. This may be due to lattice distortion and a decrement in the oxygen vacancy concentrations caused by the addition of Nd^{3+} ions. The doping of Nd^{3+} ions in BCT ceramics can also increase the bandgap and the deconvolution of the luminescence spectra unambiguously conferred it. The observed PL emission peaks at 534 nm, occur due to oxygen vacancies and further, it confirms structural changes in BCT on Nd^{3+} ions doping. In addition, the size effects (crystallite size and grain size contributions) which are responsible for bandgap increment (2.84–3.08 eV) show a blue shift, as observed not only from the UV-spectra but also obtained on PL emission (3.313–3.318 eV) studies. Also, the dielectric constant increases with increasing Nd^{3+} ion concentrations in BCT ceramics.

REFERENCES

1. M.M. Vijatović, J.D. Bobić, and B.D. Stojanović, *Sci. Sinter.* 40, 155 (2008).
2. S. Nayak, B. Sahoo, T.K. Chaki, and D. Khastgir, *RSC Adv.* 4, 1212 (2014).
3. M.K. Mahata, K. Kumar, and V.K. Rai, *Spectrochim. Acta A* 124, 285 (2014).
4. L.R. Prado, N.S. de Resende, R.S. Silva, S.M.S. Egues, and G.R. Salazar-Band, *Chem. Eng. Process.* 103, 12 (2016).
5. Ch Rayssi, S. El Kossi, J. Dhahri, and K. Khirouni, *RSC Adv.* 8, 17139 (2018).
6. S. Ray, Y.V. Kolen'ko, K.A. Kovnir, O.I. Lebedev, S. Turner, T. Chakraborty, R. Erni, T. Watanabe, G. Van Tendeloo, M. Yoshimura, and M. Itoh, *Nanotechnology* 23, 025702 (2012).

7. M. Acosta, N. Novak, V. Rojas, S. Patel, R. Vaish, J. Koruza, G.A. Rossetti, and J. Rödel, *Appl. Phys. Rev.* 4, 041305 (2017).
8. The-Long Phan, P. Zhang, D.S. Yang, T.D. Thanh, D.A. Tuan, and S.C. Yu, *J. Appl. Phys.* 113, 17305 (2013).
9. D.-D. Han, D.-Y. Lu, and X.-Y. Sun, *J. Alloy. Compd.* 576, 24 (2013).
10. A.G.A. Darwish, Y. Badr, M. El Shaarawy, N.M.H. Shash, and I.K. Battish, *J. Alloy. Compd.* 489, 451 (2010).
11. Zhonghua Yao, Hanxing Liu, Yan Liu, Wu Zhaohui, Zongyang Shen, Yang Liu, and Minghe Cao, *Mater. Chem. Phys.* 109, 475 (2008).
12. L. Padilla-Campos, D.E. Diaz-Droguett, R. Lavín, and S. Fuentes, *J. Mol. Struct.* 1099, 502 (2015).
13. T. Shi, Y. Chen, and X. Guo, *Progr Mater Sci* 80, 77 (2016).
14. E. Venkata Ramana, F. Figueiras, A. Mahajan, D.M. Tobaldi, B.F.O. Costa, M.P.F. Graça, and M.A. Valente, *J. Mater. Chem. C* 4, 1066 (2016).
15. E. Devi, B.J. Kalaiselvi, K. Madhan, D. Vanidha, S.S. Meena, and R. Kannan, *J. Appl. Phys.* 124, 8 (2018).
16. Lu Da-Yong and Yong-Shun Zheng, *J. matlet.* 223, 25 (2018).
17. H. Lemziouka, R. Moubah, F.Z. Rachid, Y. Jouane, E.K. Hlil, M. Abid, and H. Lassri, *J. Ceram. Int.* 42, 19402 (2016).
18. The-Long Phan, P.D. Thang, T.A. Ho, T.V. Manh, T.D. Thanh, V.D. Lam, N.T. Dang, and S.C. Yu, *J. Appl. Phys.* 117, 17D904 (2015).
19. G. George and S. Anandhan, *RSC Adv.* 5, 81429 (2015).
20. M. Muralidharan, V. Anbarasu, A. ElayaPerumal, and K. Sivakumar, *J. Mater. Sci.: Mater. Electron.* 26, 6875 (2015).
21. Fenggong Wang, Ilya Grinberg, and Andrew M. Rappe, *Appl. Phys. Lett.* 104, 152903 (2014).
22. M. Ganguly, S.K. Rout, T.P. Sinha, S.K. Sharma, H.Y. Park, C.W. Ahn, and I.W. Kim, *J. Alloy. Compd.* 579, 473 (2013).
23. L.V. Maneeshya, V.S. Anitha, S.S. Lekshmy, I. John Berlin Prabitha, B. Nair Georgi, P. Daniel, P.V. Thomas, and K. Joy, *J. Mater. Sci.: Mater. Electron.* 24, 848 (2013).
24. S.K. Ghosh and S.K. Rout, *Curr. Appl. Phys.* 16, 989 (2016).
25. A.S.H. Hameed, C. Karthikeyan, A.P. Ahamed, N. Thajuddin, N.S. Alharbi, S.A. Alharbi, and G. Ravi, *Sci. Rep.* 6, 24312 (2016).
26. Manjit Borah and Dambarudhar Mohanta, *J. Appl. Phys.* 112, 124321 (2012).
27. L.V. Maneeshya, P.V. Thomas, and K. Joy, *J. Optmat.* 46, 304 (2015).
28. L.V. Maneeshya, S. SujathaLekshmy, P.V. Thomas, and K. Joy, *J. Mater. Sci.: Mater. Electron.* 25, 2507 (2014).
29. Neha Sharma, Anurag Gaur, and U.K. Gaur, *J. Ceram. Int.* 40, 16441 (2014).
30. Qiaomei Sun, Gu Qilin, Kongjun Zhu, Rongying Jin, Jinsong Liu, Jing Wang, and Jinhao Qiu, *Scientific Reports* 7, 42274 (2017).
31. Kuldeep Chand Verma and R.K. Kotnala, *Mater. Res. Express* 3, 055006 (2016).
32. N. Sharma, A. Gaur, and U.K. Gaur, *Ceram. Int.* 40, 16441 (2014).
33. Wu Haidong, Pu Yongping, Zhuo Wang, and Kai Chen, *J. Matlet.* 76, 222 (2012).
34. M.-F. Lin, V.K. Thakur, E.J. Tan, and P.S. Lee, *J. Mater. Chem.* 2, 116500 (2011).
35. Alka Rania, Jayant Kolteb, and Prakash Gopalan, *J. Ceram. Int.* 44, 16703 (2018).
36. T.A.T. Sulong, R.A.M. Osman, M.S. Idris, and Z.A.Z. Jamal, *EPJ Web Conf* 162, 01050 (2017).
37. W.-B. Li, D. Zhou, B. He, F. Li, L.-X. Pang, and S.-G. Lu, *J. Alloy. Compd.* 685, 418 (2016).